

Revisit Liu and Katz (2006) and Zigunov and Charonko (2024b), Part (I): on the Equivalence of the Omnidirectional Integration and the Pressure Poisson Equation

Connor Pryce¹, Lanyu Li¹, and Zhao Pan^{*1}

¹University of Waterloo, Dept. of Mechanical and Mechatronics Engineering, Waterloo,
ON, Canada

November 6, 2024

Abstract

In this work, we demonstrate the equivalency of the Rotating Parallel Ray Omnidirectional Integration (RPR-ODI) and the Pressure Poisson Equation (PPE) for pressure field reconstruction from corrupted image velocimetry data. Building on the work by Zigunov and Charonko (2024b), we show that performing the ODI is equivalent to pursuing the minimum norm least square solution to a Poisson equation with all Neumann boundary conditions, which is an ill-posed problem. Looking through the lenses of the well-posedness of the Poisson equation, linear algebra, as well as regression and optimization, we provide a comprehensive and integrated framework to analyze ODI/PPE-based pressure field reconstruction methods. The new comprehensions on the equivalence of ODI and PPE not only can reduce the immense computational cost of ODI to that of PPE, but more importantly, unveil their shared strengths and limitations. This paves the way for further improvements in ODI/PPE-based pressure field reconstruction by utilizing the extensive literature on fast, robust elliptic solvers and their associated regularization methods. Throughout this work, we include remarks and notes offering theoretical and computational insights valuable to experimentalists. Some of these notes illustrate a “minimalist” regularization strategy, serving as “minimal reproducible examples” that provide a foundation for further refinement. Numerical experiments are presented to support and illustrate these arguments.

1 Introduction

Pressure field reconstruction from noisy velocity data obtained via Particle Image Velocimetry (PIV) or Lagrangian Particle Tracking (LPT) is an effective and non-invasive flow diagnostic strategy (Van Oudheusden, 2013). Since early development by Schwabe (1935), continuous progress

*To whom correspondence may be addressed: zhao.pan@uwaterloo.ca

in the field has resulted in a wide range of viable reconstruction methods. These reconstruction methods typically fall into one of two categories. The first category reconstruct the pressure field p by integrating the pressure gradient, $\mathbf{g}(\mathbf{u})$, obtained using the momentum equation

$$\nabla p = \mathbf{g}(\mathbf{u}) = -\rho \left[\frac{\partial \mathbf{u}}{\partial t} + (\mathbf{u} \cdot \nabla) \mathbf{u} - \nu \nabla^2 \mathbf{u} \right] \quad \text{in } \Omega, \quad (1)$$

where \mathbf{u} is the velocity field, ρ is the density, and ν is the kinematic viscosity of the fluid, respectively, for an incompressible flow.

One iconic method believed to be in this category, Omni-Directional Integration (ODI), was first introduced by [Liu and Katz \(2003, 2006\)](#), with the key idea of trying to enforce the path independence of the pressure gradient by iteratively averaging the integrated pressure along different paths starting from a virtual boundary that encloses the domain. This reconstruction method is known to be particularly robust to random noise (in the pressure gradients). However, due to the ensemble practice, the original ODI is prohibitively expensive ([Zigunov and Charonko, 2024b](#)). In addition, the reconstruction quality of ODI depends on the size and shape of the virtual boundary. To improve the computational efficiency, some strategies have been employed. Examples include using much fewer integral paths ([Dabiri et al., 2014](#)), GPU-acceleration ([Wang et al., 2019](#)), Green’s functions ([Wang and Liu, 2023](#)), and removing redundant integration ([Zigunov and Charonko, 2024a,b](#)). Since its inception, the virtual boundary has evolved from finite rectangular virtual boundary ([Liu and Katz, 2003](#)), to finite circular virtual boundary ([Liu and Katz, 2006](#)), and finally to an infinitely large virtual boundary which is the Rotating Parallel Ray Omni-directional Integration (RPR-ODI) ([Liu et al., 2016; Wang et al., 2019](#)). Due to the unbiased weighting of the ensemble integration, RPR-ODI is in general considered superior in terms of reconstruction accuracy among all other conventional ODI solvers.

The second category of methods recover the pressure field using the Pressure Poisson Equation (PPE) which is derived by applying the divergence to both sides of (1):

$$\nabla^2 p = f(\mathbf{u}) = \nabla \cdot \mathbf{g}(\mathbf{u}) = -\rho \nabla \cdot \left[\frac{\partial \mathbf{u}}{\partial t} + (\mathbf{u} \cdot \nabla) \mathbf{u} - \nu \nabla^2 \mathbf{u} \right] \quad \text{in } \Omega, \quad (2)$$

where $f(\mathbf{u}) = \nabla \cdot \mathbf{g}(\mathbf{u})$ is the data of the Poisson equation. Invoking the vector calculus identity $\nabla \cdot (\nabla^2 \mathbf{u}) = \nabla^2 (\nabla \cdot \mathbf{u})$, the viscous term in (2) vanishes if the flow is incompressible. Although the Poisson equation benefits from superior numerical stability, ease of implementation, and high computational efficiency, experimentation using various numerical methods ([Charonko et al., 2010; Sperotto et al., 2022; Zhang et al., 2020](#)) has shown that reconstruction may suffer, more or less, when subject to noisy velocimetry data.

Over the years, it has long been debated which of the two categories is better for pressure reconstruction, particularly the ODI versus PPE. Some have claimed that the ODI is fundamentally different and far more accurate than solving the PPE (e.g., [Liu and Moreto \(2020\)](#)); while other studies have observed similar reconstruction accuracy between the ODI and PPE ([McClure and Yarusevych, 2017b](#)). This debate has been filled with confusion and conflicting results until a recent breakthrough by [Zigunov and Charonko \(2024a,b\)](#), while trying to improve the computational efficiency of ODI. In a series of works, [Zigunov and Charonko \(2024a,b\)](#) reformulated the iterative integration process of the ODI into a system of linear equations resembling the discretized PPE, alluding to a deep connection between the ODI and PPE.

Inspired by the recent progress of [Zigunov and Charonko \(2024a,b\)](#), in this work, we show that indeed the RPR-ODI is equivalent to a special case of PPE, and that the reason for the perceived difference in robustness between ODI and PPE is all in the details of numerical implementation and

regularization. These findings will end a long debate about which method is better, and reduce the computational cost of the ODI to match that of the PPE while preserving the robustness observed in ODI. Additionally, and more importantly, we establish a unified framework to analyze ODI/PPE-based pressure field reconstruction through the lenses of the well-posedness of the elliptic equation, linear algebra, statistics, and optimization. While the tools used in this work are well-established, we aim to provide an integrated analysis offering comprehensive insights and hopefully inspire new, effective regularization techniques for faster, more accurate, and robust pressure reconstruction.

The work is organized as follows. Sect. 2 establishes the equivalency between the ODI and PPE by drawing on the results in [Zigunov and Charonko \(2024b\)](#). Sect. 3 reviews the major results of the well-posedness of the Poisson equation in the continuous and discrete settings, which serves as a ground for further analysis. In Sect. 4, we unveil the precise meaning of the solution from the ODI or the corresponding ill-posed PPE. Sect. 5 gives insights into the robustness of the ODI/PPE-based pressure field reconstruction, followed by Sect. 6, where the singularity of the one-point Dirichlet setup for a PPE is discussed. We also provide some elementary notes on the computational practices in Sect. 7, before demonstrating synthetic experiments supporting our major arguments throughout the work in Sect. 8. We conclude this work by recapping the shared fundamentals of the ODI and PPE in Sect. 9, which also infer perspectives for future improvements.

2 Equivalency of ODI and PPE

In this section, we demonstrate that using the RPR-ODI to reconstruct the pressure field is equivalent to pursuing a solution to a PPE with all Neumann boundary conditions.

The recent advancement of ODI ([Zigunov and Charonko, 2024a](#)) removed the redundant ensemble integration along different paths by examining the integral at each cell in the domain and on the boundaries. The resulting iterative pressure solver named “Iterative Matrix ODI (I-MODI)” by the authors is significantly faster than traditional versions of ODI. This work showed that at convergence, the accuracy of the I-MODI solver is typically very close to or slightly better than the Rotating Parallel Ray ODI (RPR-ODI), which is considered the most accurate among all of the traditional ODI solvers ([Liu et al., 2016](#); [Wang et al., 2019](#)). More importantly, it was shown that when given the same corrupted velocimetry data, the reconstruction error from the I-MODI and high-resolution RPR-ODI are almost identical. This is strong evidence suggesting that the matrix ODI approaches the limit of the traditional ODI when computed with high resolution.

A follow-up work ([Zigunov and Charonko, 2024b](#)) examined the fixed point of the I-MODI iteration and found that at convergence, ODI can be computed by solving a linear system of the form

$$\mathcal{L}\mathbf{p} = \mathbf{b}, \tag{3}$$

with \mathbf{p} being the pressure field to be solved, \mathbf{b} the data, and \mathcal{L} is the discretized Laplacian. This linear system does not have to be solved iteratively and is dubbed as “One-Shot Matrix ODI” (OS-MODI). When solved for the pressure field, it was shown that OS-MODI and I-MODI result in the same pressure reconstruction as RPR-ODI, with an $O(10^3)$ to $O(10^6)$ times improvement in speed on their test cases.

Beyond the robustness and high computational efficiency, the reformulation in [Zigunov and Charonko \(2024b\)](#) suggests strong connections between PPE and ODI through the numerical implementation of \mathcal{L} and \mathbf{b} in (3). As an example, [Zigunov and Charonko \(2024b\)](#) showed that on a 2D uniform grid, at the convergence of ODI, the pressure at an interior nodal point ($p_{i,j}$) can be

evaluated as

$$p_{i,j} = \frac{1}{4} (p_{i+1,j} + p_{i-1,j} + p_{i,j+1} + p_{i,j-1}) + \frac{1}{8} h (g_x|_{i-1,j} - g_x|_{i+1,j} - g_y|_{i,j+1} + g_y|_{i,j-1}), \quad (4)$$

where $g_x|_{i,j}$ and $g_y|_{i,j}$ are the pressure gradients in x and y directions obtained from the momentum equations using the measured velocity evaluated at location (x_i, y_j) , and h is the grid spacing.¹ Rearranging (4) leads to

$$-4p_{i,j} + p_{i+1,j} + p_{i-1,j} + p_{i,j+1} + p_{i,j-1} = h^2 \left(\frac{g_x|_{i+1,j} - g_x|_{i-1,j}}{2h} + \frac{g_y|_{i,j+1} - g_y|_{i,j-1}}{2h} \right) = h^2 f_{i,j} \quad (5)$$

where the data $f_{i,j} = (\partial_x g_x + \partial_y g_y)|_{i,j}$ is evaluated by the second order central difference (e.g., $\partial_x g_x|_{i,j} = \frac{1}{2h} (g_x|_{i+1,j} - g_x|_{i-1,j})$). This result is the familiar five-point finite difference scheme for the discrete Laplacian (Chen, 2020; Thomas, 2013a,b), denoted as $(-4, 1, 1, 1, 1)$ where each value corresponds to the pressure coefficients seen in the left hand side of (5). The layout of the nodes and the stencil shown in (5) is illustrated in Fig. 1.

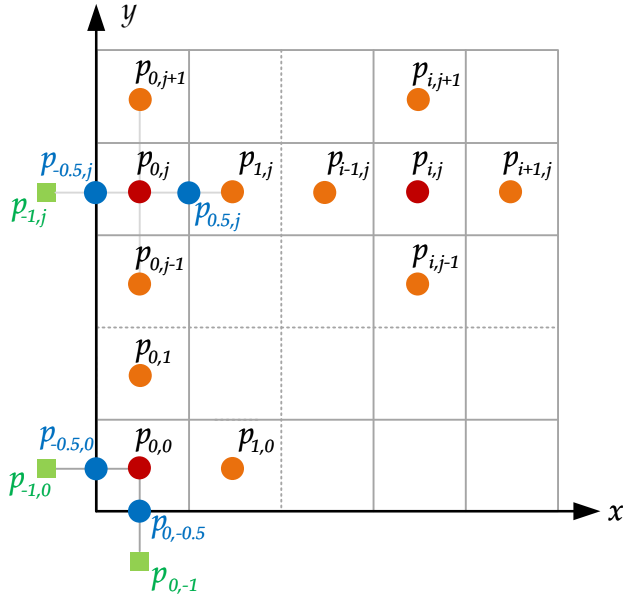


Figure 1: Cell-centered layout of the discretized domain. The green squares indicate the ghost points.

Likewise, Zigunov and Charonko (2024b) also derived

$$p_{0,j} = \frac{1}{3} (p_{1,j} + p_{0,j+1} + p_{0,j-1}) + \frac{1}{3} h \left(-\frac{g_x|_{0,j} + g_x|_{1,j}}{2} + \frac{g_y|_{0,j-1} - g_y|_{0,j+1}}{2} \right), \quad (6)$$

which describes the treatment of the nodes on the boundary. To derive this stencil by finite differences, we start by introducing a ghost node on a cell-centered grid located a distance of $h/2$ away from the edge of the domain. Then we enforce a Neumann condition on the boundary (e.g., specify the value of $\mathbf{n} \cdot \nabla p$ at $(x_{-0.5}, y_j)$) using the following first-order scheme:

$$-\mathbf{n} \cdot \nabla p|_{-0.5,j} = g_x|_{-0.5,j} = \frac{p_{0,j} - p_{-1,j}}{h}. \quad (7)$$

¹The notation for the pressure gradient at, for example, center and west nodal points are $f_x(C)$ and $f_x(E)$, respectively, in Zigunov and Charonko (2024b); while, in the current work, they are denoted as $g_x|_{i,j}$ and $g_x|_{i+1,j}$, respectively.

We compute $g_x|_{0.5,j}$ by linearly interpolating between $g_x|_{0,j}$ and $g_x|_{1,j}$:

$$g_x|_{0.5,j} = \frac{g_x|_{0,j} + g_x|_{1,j}}{2}, \quad (8)$$

and evaluate the data $f_{0,j}$ by

$$f_{0,j} = \frac{g_x|_{0.5,j} - g_x|_{-0.5,j}}{h} + \frac{g_y|_{0,j+1} - g_y|_{0,j-1}}{2h}. \quad (9)$$

Substituting (7) and (8) into (9), and then (9) into (5) and setting $i = 0$ recover (6). The stencil indicated in (6) can be denoted as $(-3, 1, 1, 1)$ (see also in Fig. 1). A similar treatment using ghost points at the corners of the domain will produce stencil $(-2, 1, 1)$, which also matches Zigunov and Charonko (2024b), and is one of the classic implementations of boundaries and corners for a Neumann problem (Chen, 2020; Thomas, 2013b). The above numerical analysis leads to the following argument:

Remark 2.1 (ODI \equiv PPE). *Using the ODI to reconstruct the pressure field from the pressure gradient is (numerically) equivalent to solving a PPE with all Neumann boundary conditions.*

Remark 2.1 represents the main result of this work. The discussions that follow primarily build on established results from the well-posedness of Poisson equations, estimation theory, statistics, and numerical analysis. Together, they provide a unified framework for analyzing and refining ODI/PPE-based methods for pressure field reconstruction.

The above combination of corner, wall, and interior stencils is a good choice for the Neumann problem of the Poisson equation; however, it is not the only one. Stencil construction and the combinations of stencils used is very important and naive numerical treatments could lead to a more ill-posed and/or ill-conditioned system with singularities. Employing other numerical methods (e.g., finite element, finite volume, or meshless methods) may also yield stencils equivalent or similar to the ones mentioned above (e.g., (4) and (6)). It is also possible that these methods may even produce better numerical schemes; however, we will leave this topic to future studies. In this work, we focus on establishing the equivalency of ODI and PPE (dubbed as ODI \equiv PPE) using a simple finite difference scheme following Zigunov and Charonko (2024b) and exposing the fundamental mathematical foundations of their shared advantages (e.g., robustness) and disadvantages, hopefully, inspiring general strategies for further improvement.

Solving the singular or ill-posed system (3) is non-trivial, as \mathcal{L} , which we refer to as \mathcal{L}_N from now on with the subscript $[\cdot]_N$ to denote the Neumann problem, is rank-deficient, thus, non-invertible. If a solution to (3) exists, it is not unique; not to mention that a solution may not exist at all. In the case of Zigunov and Charonko (2024b), a conjugate gradient (CG) method with a carefully chosen stopping criteria was used to solve the singular system, and the solution was shifted to match the reference pressure at a given location in the domain or on the boundary. The use of CG and appropriate terminating criteria (i.e., maximum iterations and tolerance) is subtle yet crucial for several reasons, which will be elaborated upon in the following sections.

With the equivalence between the RPR-ODI and the PPE established, this work will now focus on exploring key theoretical aspects of ODI/PPE for pressure reconstruction and addressing several interesting questions, for example: (i) what is the precise sense of the solution obtained from the ODI or equivalent PPE of (3) (see Sect. 3 and 4)? (ii) Why is ODI/PPE robust against random noise, and why does it appear to perform particularly well with high-resolution data (see Sect. 5)? (iii) If the ODI and PPE are equivalent, why do some observe that the ODI demonstrates greater robustness compared to certain implementations of the PPE (see Sect. 6)? (iv) What insights can we gain from ODI/PPE, and how can we make further improvements (see the notes and remarks scattered in the rest of the current work)?

3 Well-posedness of the Neumann Problem of the Poisson Equation

To better understand why some have reported major differences in the performance between the ODI and PPE, as well as the shared robustness of traditional ODI methods (Liu and Katz, 2006; Wang et al., 2019; Wang and Liu, 2023) and the fast implementations by Zigunov and Charonko (2024a,b), we must first understand the intrinsic ill-posedness of the Neumann problem of the Poisson equation and how the compatibility condition is essential for a valid pressure reconstruction.

3.1 The Compatibility Condition and the Existence of the Solution

The Neumann problem of the Poisson equation (2) is equipped with boundary conditions

$$\mathbf{n} \cdot \nabla p = g_n \quad \text{on} \quad \partial\Omega, \quad (10)$$

which are readily available by evaluating the momentum equation on the boundaries. If a solution exists, it is unique up to a constant, and requires the following compatibility condition to be satisfied

$$\int_{\Omega} f dV - \int_{\partial\Omega} g_n dS = 0. \quad (11)$$

This condition can be intuitively understood in the context of diffusion at steady state with distributed generation. The compatibility condition says that at steady state, the total flux (i.e., $\int_{\partial\Omega} g_n dS$) through the boundary must be balanced by the total generation in the domain (i.e., $\int_{\Omega} f dV$).

If the compatibility condition (11) is not satisfied, the solution to the Neumann problem of the Poisson equation does not exist and this is often the case when the data are contaminated. If we denote the corrupted data in the domain as $\tilde{f} = f + \epsilon_f$ and on the Neumann boundary as $\tilde{g}_n = g_n + \epsilon_{g_n}$, where ϵ_f and ϵ_{g_n} are the error in the corresponding true values of f and g_n respectively, (11) becomes

$$\int_{\Omega} \tilde{f} dV - \int_{\partial\Omega} \tilde{g}_n dS = \epsilon_c, \quad (12)$$

where ϵ_c is a residual. It is important to note that ϵ_c may not vanish depending on how \tilde{f} and \tilde{g}_n are computed or prescribed. If \tilde{f} is precisely computed as $\tilde{f} = \nabla \cdot \tilde{\mathbf{g}}$ using a consistent² numerical method, the compatibility condition is satisfied automatically by the divergence theorem. Otherwise, the compatibility condition could be violated. This can be seen by subtracting (11) from (12), which yields

$$\epsilon_c = \int_{\Omega} \epsilon_f dV - \int_{\partial\Omega} \epsilon_{g_n} dS.$$

where $\epsilon_c \neq 0$ unless the total error in the domain is somehow equal to the total error on the boundary. This could happen in some scenarios. For example, ϵ_f is exactly carried from $\nabla \cdot \epsilon_{\mathbf{g}}$ by consistent computation, and the divergence theorem demands $\epsilon_c = 0$. Or, both ϵ_f and ϵ_{g_n} happened to be mean zero noise. Interestingly, this is the case in some studies where mean zero Gaussian noise is introduced to \mathbf{g} to generate synthetic data. The higher the spatial resolution of the data, the better the compatibility condition is satisfied *statistically*. However, the real experimental data may not accommodate this assumption.

²Consistent and consistency here is a term in the context of the numerical analysis. A consistent numerical discretization refers to a numerical method that recovers the corresponding continuous problem exactly as the grid spacing of discretization approaches zero.

In other words, the solution to the contaminated Neumann problem

$$\begin{aligned}\nabla^2 \tilde{p} &= \tilde{f} & \text{in } \Omega \\ \nabla \tilde{p} \cdot \mathbf{n} &= \tilde{g}_n & \text{in } \partial\Omega,\end{aligned}$$

may not exist because the contaminated data \tilde{f} and \tilde{g}_n are conflict with each other such that $\epsilon_c \neq 0$ in (12). To address this issue, some regularization can be used to satisfy the compatibility condition and ensure the existence of the solution, which will be discussed further in later sections.

Now looking at the discretized setting, the corresponding linear system for the Neumann problem of the Poisson equation is

$$\mathcal{L}_N \mathbf{p} = \mathbf{b}_N. \quad (13)$$

Generally speaking, the existence of a solution to the singular system (13) requires that the data vector \mathbf{b}_N must be in the column space of \mathcal{L}_N :

$$\mathbf{b}_N \in \text{Col}(\mathcal{L}_N), \quad (14)$$

which is the compatibility condition in the discretized setting. If $\mathbf{b}_N \notin \text{Col}(\mathcal{L}_N)$, the incompatible data renders an inconsistent³ system of (13) that has no solution.

Since the vector \mathbf{b}_N in (13) embeds the data f and g_n of the Poisson problem, it also must reflect the continuous compatibility condition of (11). For (13), the balance of total generation $\int_{\Omega} f dV$ and total flux $\int_{\partial\Omega} g_n dS$ manifests itself as

$$\sum_{i=1}^m b_{Ni} = 0, \quad (15)$$

where m is the dimension of \mathcal{L}_N , and b_{Ni} is the i -th element of \mathbf{b}_N . Satisfying (15), which is equivalent to asking \mathbf{b}_N being mean zero (i.e., $\bar{\mathbf{b}}_N = \frac{1}{m} \sum_{i=1}^m \mathbf{b}_{Ni} = 0$), will automatically ensure (14) due to the unique property of \mathcal{L}_N . To see why the discrete Laplacian (\mathcal{L}_N) for the Neumann problem has this property, we can look at the problem through the lens of linear algebra. If the discretization of the Laplacian is done correctly, the null space of \mathcal{L}_N should be equal to the one vector, i.e. $\text{Null}(\mathcal{L}_N) = \mathbf{1}$. Since a valid solution to (13) requires $\bar{\mathbf{b}}_N$ to be orthogonal to the null space of \mathcal{L}_N , \mathbf{b}_N must be orthogonal to the one vector: $\mathbf{1}^T \mathbf{b}_N = 0$, which exactly recovers (15).

For the corresponding corrupted problem of (13)

$$\mathcal{L}_N \tilde{\mathbf{p}} = \tilde{\mathbf{b}}_N, \quad (16)$$

the data vector $\tilde{\mathbf{b}}_N$ is contaminated by noise and it may not be mean zero and, thus, $\tilde{\mathbf{b}}_N \notin \text{Col}(\mathcal{L}_N)$. Even small error in $\tilde{\mathbf{b}}_N$, numerical and/or experimental, can knock the vector out of the column space of \mathcal{L}_N , breaking the compatibility condition and rendering any ‘direct result’ from a numerical solver as nonsense. To solve the incompatible/inconsistent problem, one has to regularize \mathcal{L}_N and/or $\tilde{\mathbf{b}}_N$ so that the data is compatible and a valid solution exists.

³Consistent and inconsistent here, in the context of linear algebra, refers to a linear system that has a solution. In the context of pressure reconstruction based on the Poisson equation, an inconsistent system is rooted in the incompatibility of the corrupted Neumann problem of the Poisson equation. In this work, we use consistency and compatibility interchangeably when discussing the existence of the solution in discretized or continuous settings.

3.2 The Uniqueness of the Solution

If the compatibility condition (11) is satisfied, p solves the problem of (2) and (10), then $p + p_0$ is also a solution, where p_0 is an arbitrary constant. In other words, there are infinitely many solutions to a compatible Neumann problem, and these solutions are unique up to an additive constant.

In the discrete setting, the non-uniqueness of the solution is reflected by the fact that \mathcal{L}_N , if properly constructed, is rank deficit by one and $\text{Null}(\mathcal{L}_N) = \mathbf{1}$. This means that the linear system (3) is underdetermined, and the solution to (3), if it exists, is again unique up to a constant, if and only if the compatibility condition ($\mathbf{b}_N \in \text{Col}(\mathcal{L}_N)$ or $\tilde{\mathbf{b}}_N = 0$) is satisfied.

4 Ill-posed Neumann Problem, Conjugate Gradients, and Minimum Norm Least Squares Solution

One may wonder how Zigunov and Charonko (2024b) solved the ill-posed system of (16), where \mathcal{L}_N is indefinite and $\tilde{\mathbf{b}}$ may not satisfy the compatibility condition. By answering this question, we give a precise interpretation of the output from RPR-ODI.

The key to the success of Zigunov and Charonko (2024b) lies in the remarkable property of CG: Due to the fact that \mathcal{L}_N is symmetric and semi-definite, running CG on the underdetermined system of (13), converges *towards* the minimal norm solution. Classic analysis on this topic can be found in Kammerer and Nashed (1972); Hestenes (2012). This means that the *results* from the ODI methods are equivalent to *pursuing* a ‘solution’ to the following constrained optimization problem:

$$\begin{aligned} \min_{\mathbf{p}} \mathcal{J} &= \|\mathbf{p}\|_2 \\ \text{s.t. } \mathcal{L}_N \mathbf{p} &= \mathbf{b}_N. \end{aligned} \tag{17}$$

In the case where the data is contaminated, $\tilde{\mathbf{b}}_N$ can corrupt the constraints in (17) by breaking the compatibility condition as described in Sect. 3, and the exact solution to the above optimization problem does not exist as the constraint cannot be satisfied. As a result, directly running CG on the inconsistent system (16) may diverge depending on the starting point, stopping criteria, and the specific variant of the CG methods used. Despite this, one could still pursue a $\hat{\mathbf{p}}$ that best satisfies the ‘constraint’ $\mathcal{L}_N \mathbf{p} = \tilde{\mathbf{b}}_N$ (e.g., minimizing the residual $\mathbf{r} = \mathcal{L}_N \hat{\mathbf{p}} - \tilde{\mathbf{b}}_N$ in the sense of some norm), and this is perhaps the best solution in a particular sense (see Sect. 5 for more detailed elaboration).

In general, the most straightforward solution to this inconsistent singular system can be achieved as

$$\hat{\mathbf{p}} = \mathcal{L}_N^\dagger \tilde{\mathbf{b}}, \tag{18}$$

where \mathcal{L}_N^\dagger is the Moore-Penrose pseudo-inverse of \mathcal{L}_N . This solution is a Minimum Norm Least Squares (MNLS) solution and carries several remarkable properties. We provide a brief interpretation, in the context of pressure field reconstruction, following the classic results of generalized inverse (Campbell and Meyer, 2009; Gallier and Quaintance, 2020) with following remarks:

Remark 4.1 (least squares solution). $\hat{\mathbf{p}}$ is a least squares solution to $\mathcal{L}_N \mathbf{p} = \tilde{\mathbf{b}}_N$. This means that $\hat{\mathbf{p}}$ overall matches the contaminated data $\tilde{\mathbf{b}}_N$ best with respect to the L^2 -norm.

This (ordinary) least squares solution $\hat{\mathbf{p}}$ can also be interpreted as an attempt to the Best Linear Unbiased Estimator (BLUE). It typically performs well, statistically, assuming that *high-resolution* data is contaminated by *uncorrelated mean-zero random noise* in $\tilde{\mathbf{b}}_N$. However, the ‘optimality’ of the BLUE is fragile in several ways due to these strong assumptions (see Sect. 5 for more

discussions). In addition, we may argue that different versions of ODI (with various arrangements of the sizes and shapes of virtual boundaries) correspond to weighted least squares. However, the weights are dictated by the rays, due to the choice of virtual boundaries, instead of the nature of the data or the flow being studied.

Remark 4.2 (minimal norm solution). *$\hat{\mathbf{p}}$ is a minimal norm solution. That is, $\hat{\mathbf{p}}$ has the lowest energy (measured by the L^2 -norm) among all other possible least square solutions. This recovers the intention of (17), and automatically requires that $\hat{\mathbf{p}}$ be mean-zero.*

This minimal norm feature and mean-zero solution outcome are of significance in terms of the robustness of the reconstruction (see Remark 5.2 for more details).

Remark 4.3 (solution of minimal correction). *$\hat{\mathbf{p}}$ is an outcome of applying a minimal correction to the corrupted data $\tilde{\mathbf{b}}_N$, achieved by orthogonal projection.*

This can be explained by observing the fact that $\hat{\mathbf{p}}$ is also an *exact* solution of $\mathcal{L}_N \mathbf{p} = \mathcal{L}_N \mathcal{L}_N^\dagger \tilde{\mathbf{b}}_N$. $\mathcal{P} = \mathcal{L}_N \mathcal{L}_N^\dagger$ projects $\tilde{\mathbf{b}}_N$ into the column space of \mathcal{L}_N satisfying the compatibility condition, and removing the error in $\tilde{\mathbf{b}}_N$ that violates the compatibility condition. In addition, \mathcal{P} is orthogonal; thus, the erroneous component removed from $\tilde{\mathbf{b}}_N$ by \mathcal{P} is the smallest possible with respect to the L^2 -norm. The minimal action of correction is often a good, if not the best, choice when no additional assumption is made or *a priori* is available.

Remark 4.4 (normal equation). *One may avoid direct computation of pseudo-inverse using the normal equation. This can be seen by noticing that $\hat{\mathbf{p}}$ is an exact solution of $\mathcal{L}_N^\top \mathcal{L}_N \mathbf{p} = \mathcal{L}_N^\top \tilde{\mathbf{b}}_N$, which is the normal equation of $\mathcal{L}_N \mathbf{p} = \tilde{\mathbf{b}}_N$.*

In addition, it is easy to see that the right hand side of the normal equation $\mathcal{L}_N^\top \tilde{\mathbf{b}}_N$ is in the column space of \mathcal{L}_N by projection, and satisfies the compatibility condition given any $\tilde{\mathbf{b}}_N$. This interpretation is attractive as it facilitates stable convergence for numerical computations.

Remark 4.5 (well-posed problem). *$\hat{\mathbf{p}}$ always exists and is unique.*

The challenge of the original ill-posed Neumann problem for the Poisson equation is no longer an issue, and the corresponding MNLS problem is now well-posed. The significance of this feature is self-evident.

Remark 4.6 (no curl-free correction involved). *$\hat{\mathbf{p}}$ is precisely a minimum norm least squares solution, and it does not perform any curl-free correction to $\tilde{\mathbf{g}}$.*

The ODI methods are motivated by the gradient theorem, which states that the line integral along the gradient field of a scalar (e.g., contaminated pressure gradients) should be path-independent. Although the path independence property demands curl-free pressure gradients ($\nabla \times \tilde{\mathbf{g}} = \mathbf{0}$), the minimum norm least squares solution does not result in the ODI achieving curl-free correction to $\tilde{\mathbf{g}}$.

5 On the Robustness of ODI/PPE

The above interpretation in Sect. 4 illustrates the actual intention of the ODI methods and the exact sense of the solution: a minimum norm least squares solution. Despite this, one may still wonder, what is the fundamental mechanism behind the robustness of the ODI (and the equivalent PPE)? Perhaps the most obvious explanation to the robustness of the ODI is that the ensemble

averaging practice of the traditional ODI algorithms work to cancel out the random noise. However, this is only one way—but not necessarily a fundamental way—to look at it: recall that the matrix ODI methods in [Zigunov and Charonko \(2024a,b\)](#) do not apply any ensemble averaging and achieve the same accuracy and robustness as the conventional RPR-ODI.

Extending the comprehensions in Sect. 4, we may gain insights into why the ODI/PPE is robust against random noise from various perspectives, which may inspire improvements within easy reach by leveraging some classic results in approximation, statistics, regularization, and data assimilation. We keep notes herein as follows, in the order of importance in the authors’ view, which could be subjective.

Remark 5.1 (guaranteed compatibility). *RPR-ODI implicitly (and iteratively) seeks an orthogonal projection to correct the data to guarantee the compatibility of the Neumann problem of the Poisson equation.*

This ensures the existence of the solution (see Remarks 4.3 and 4.5, as well as Sect. 3). Upon proper discretization, the solution out of ODI does not blow up.

Remark 5.2 (eliminate constant bias). *The minimal norm solution eliminates the constant bias in the reconstructed pressure—which is the lowest mode and often the most hostile error—if one can assume p is mean zero.*

If we can assume p is mean-zero, the minimal norm solution demands that $\bar{\hat{\mathbf{p}}} = 0$ (see Remark 4.2). Consequently, the error in $\hat{\mathbf{p}}$ is also mean-zero, effectively eliminating the constant bias (i.e., the lowest Fourier mode) in ϵ_p . This constant bias in ϵ_p is caused by low-frequency error in the data, which are the most dangerous modes being amplified through reconstruction ([Faiella et al., 2021](#)). In most cases, we may always be able to assume p is mean-zero as pressure is a relative value. Strictly for solving, we can use this assumption and shift the pressure to match some non-mean-zero reference value after the reconstruction.

Remark 5.3 (intrinsic low pass filter). *The intrinsic low-pass filter effect of (implicitly) integrating the Laplacian or pressure gradients eliminates noise in the data $\tilde{\mathbf{g}}$ and $\tilde{\mathbf{f}}$.*

This property is also independent to the numerical methods/algorithm. It is rooted in the nature of integration (i.e., ∇^{-2} for f or ∇^{-1} for \mathbf{g} , and see [De Kat and Van Oudheusden \(2012\)](#); [Faiella et al. \(2021\)](#); [Li et al. \(2024b\)](#) for some discussions) and one may recall the heuristic that the integration of a noisy signal is almost always smoother than the original noisy signal.

Remark 5.4 (BLUE). *$\hat{\mathbf{p}}$ from ODI could be BLUE (see Remark 4.1), provided that the following three conditions are satisfied: the noise in the data $\tilde{\mathbf{b}}$ is uncorrelated, mean zero, and has equal variances σ_b^2 ([Henderson, 1975](#)).*

Looking through this statistical lens, we can gain additional insights and inspire easy improvements to the ODI/PPE by some classic results. We list some here in the context of pressure reconstruction for convenience. For example, the unbiasedness of BLUE implies that $\hat{\mathbf{p}}$ ‘faithfully’ carries the statistics of the noise in $\tilde{\mathbf{b}}_N$: $\mathbb{E}[\hat{\mathbf{p}} - \mathbf{p}] = \mathbf{0}$, and the covariance of the estimate is

$$\text{Cov}[\hat{\mathbf{p}}] = \sigma_b^2 (\mathcal{L}_N^\dagger)^\top \mathcal{L}_N^\dagger, \quad (19)$$

where σ_b^2 is the standard deviation of the noise in $\tilde{\mathbf{b}}_N$. Equation (19) effectively gives an uncertainty quantification, given that σ_b^2 can be assumed as a constant and is accessible.

The *consistency*⁴ of BLUE suggests that larger data (e.g., from higher-resolution experiments) would allow us to better recover the unknown true value of the pressure field (an alternative justification by Fourier analysis can be found in Li et al. (2024b)). Interestingly, the consistency of BLUE immediately recovers the major result in Liu and Moreto (2020): if the pressure gradient is contaminated by mean-zero noise, the error in the pressure reconstruction converges to zero as the resolution of the data increases to infinitely high.

Given the fact that realistic PIV data are typically correlated and the uncertainty varies greatly over the domain, precise BLUE is not guaranteed by ODI methods (including RPR-ODI and matrix-ODI methods). Moreover, the uncertainty quantification suggested in (19), strictly speaking, is not valid. Instead, ODI or PPE achieves a statistically sub-optimal solution. This understanding also allows us to comment on the impact of how noise is introduced when generating synthetic data for validation. One can introduce noise to the pressure gradient field (\mathbf{g}) or to the velocity field (\mathbf{u}), as we will soon demonstrate in Sects. 8.1 and 8.2, respectively. When point-wise Independent and Identically Distributed (IID) random noise is added to \mathbf{g} , the solution from RPR-ODI and PPE is BLUE. This practice, commonly seen in literature, is proper for investigating the properties of a pressure solver itself; however, it artificially accommodates the requirements for BLUE and favors the BLUE-orientated solver, despite being not realistic for validation.

From this estimation and BLUE perspective, we can see some obvious strategies to improve ODI/PPE-based pressure solvers. When the error in the PIV is considered flow-dependent (usually not IID), and additive to \mathbf{u} —instead of additive \mathbf{g} —it is possible to use weighted pseudo-inverse to achieve BLUE (Henderson, 1975). This approach is already demonstrated in Zhang et al. (2020). Their tests show an approximate 20% improvement in accuracy compared to using regular pseudo-inverse.

For further improvement, one may consider the classical idea of trading off the requirement of linearity and/or unbiasedness for a more accurate estimate of \mathbf{p} , which is possible by the familiar Tikhonov regularization (Hoerl and Kennard, 1970; Hastie et al., 2009). In fact, improvement by regularization is almost always guaranteed upon proper choice of regularization method and parameters (Hastie et al., 2009), but we will leave a detailed discussion on this topic for future discussions.

From the above remarks in this section, we may finally see why the ODI has been reported to be robust against random noise and how to make further improvements.

6 Singular Poisson problem with one point Dirichlet condition

To regularize the Neumann problem of the Poisson equation such that it is well-posed, one can simply introduce Dirichlet conditions: Prescribing the Dirichlet (boundary) condition even at one point (i.e., enforcing $p(\mathbf{x}_0) = p_0$ as the reference pressure at a specific location \mathbf{x}_0 in the domain or on the boundary) is enough to guarantee the a unique solution if it exists.⁵ Since the pressure gradient is not specified at the location where the Dirichlet condition is prescribed, the solution itself dictates $\mathbf{n} \cdot \nabla \tilde{p}$ to satisfy the compatibility condition. This is particularly problematic due to the singularity at the Dirichlet point, which will be elaborated on shortly.

In the discrete context, with the single-point Dirichlet condition, the corresponding linear system

⁴Consistency here is in the context of statistics. An estimator of a given parameter is said to be consistent if it converges in probability to the true value of the parameter as the sample size tends to infinity.

⁵An alternative choice is to prescribe the mean pressure field being a constant, which is potentially a more robust choice. We will focus on the one-point Dirichlet case in this work.

for the one-point Dirichlet problem is

$$\mathcal{L}_1 \mathbf{p} = \mathbf{b}_1. \quad (20)$$

This system can be constructed by replacing one corresponding line of the original underlying Neumann problem of (13) with $p(\mathbf{x}_0) = p_0$. \mathcal{L}_1 is invertible and thus no matter how much \mathbf{b}_1 is contaminated, \mathbf{b}_1 is always in the range of \mathcal{L}_1 , and the solution to (20) exists and is unique.

Despite being direct and exact, this treatment is often not ideal in practice due to the singularity (‘free’ slope near the Dirichlet point as mentioned above) in addition to the potential large condition number of \mathcal{L}_1 . As mentioned, special care must be taken to ensure the data \tilde{f} and \tilde{g}_n are computed or prescribed such that the compatibility condition is satisfied for the original underlying Neumann problem. Particularly, if proper computation is not implemented to develop (13) and (20), the incompatible data of \mathbf{b}_N in (13) will still remain in \mathbf{b}_1 and the solution to (20) can drift resulting in significant error. This phenomenon can be seen in some Poisson solvers with point Dirichlet conditions where the solution floats with a spike (high slope around) at the Dirichlet point. In this case, any ‘generation’ (\tilde{f}) that is not balanced by the total ‘flux’ (\tilde{g}_n) on the Neumann boundaries must go through the Dirichlet point. This can lead to excessively high ‘flux’ at the location where the reference pressure (Dirichlet condition) is prescribed, and hence, the floating pressure reconstruction. This is likely a reason for the poor performance of some PPE-based pressure field reconstructions observed in the literature. The most fundamental choice to resolve this compatibility issue is perhaps to leverage the divergence theorem and use proper stencils:

Note 6.1 (ensure compatibility by the divergence theorem). *One can compute the data \tilde{f} exactly as $\tilde{f} = \nabla \cdot \tilde{\mathbf{g}}$ and use $\mathbf{n} \cdot \nabla p = \tilde{g}_n = \mathbf{n} \cdot \tilde{\mathbf{g}}$ as Neumann boundary conditions with a consistent numerical scheme.*

This practice ensures that $\tilde{g}_n = \mathbf{n} \cdot \tilde{\mathbf{g}}$ and $\tilde{f} = \nabla \cdot \tilde{\mathbf{g}}$ are always compatible by the divergence theorem, no matter how much $\tilde{\mathbf{g}}$ is contaminated. Since \tilde{f} is directly computed from $\nabla \cdot \tilde{\mathbf{g}}$, given any enclosed subdomain within the domain, the compatibility condition is satisfied locally and globally.

This suggests a simple guideline for best practice. When more accurate or better boundary conditions are available (e.g., $g_n = 0$ at a wall or in the far field, or accurate Dirichlet boundary conditions measured by transducers or inferred by the Bernoulli’s principle), one should regularize or correct $\tilde{\mathbf{g}}$ first, then compute \tilde{f} based on the corrected $\tilde{\mathbf{g}}$ before applying the boundary conditions. This subtle practice could effectively improve the reconstruction performance by naturally satisfying the compatibility condition of the underlying Neumann problem of the Poisson equation. In the following section, we will suggest some additional simple regularization to ensure compatibility.

7 Notes for Practical Computation

The computation of the pseudo-inverse or minimum norm least squares solution for an inconsistent indefinite system is not trivial. Typical methods involve using Singular Value Decomposition (SVD), Complete Orthogonal Decomposition (COD), and some iterative methods such as CG with some constraints (e.g., MATLAB’s `pinv()`, `lsqminnorm()`, and `pcg()`, respectively). We will discuss SVD-based solution in this section, as it is foundational to the theories of pseudo-inverse and is also practically useful. We will also use CG as an interesting example since it is shown in [Zigunov and Charonko \(2024b\)](#) to be successful in their tests and CG is considered the essential solver for large sparse systems. However, there are some subtle yet critical caveats regarding this practice: If the data \mathbf{b}_N is consistent (i.e., $\mathbf{b}_N \in \text{Col}(\mathcal{L}_N)$), CG converges to the MNLS solution. If the data $\tilde{\mathbf{b}}_N$ is inconsistent (i.e., $\tilde{\mathbf{b}}_N \notin \text{Col}(\mathcal{L}_N)$), the classical CG may converge *towards* the MNLS solutions if a proper initial guess is chosen; however, the intended MNLS solution will not be exactly recovered,

and the iteration may diverge (Lim et al., 2024) after certain number of iterations. In this section, we list some notes on the computational practices for the experimentalists.

Note 7.1 (enforce mean-zero data). *Correct $\tilde{\mathbf{b}}_N$, by enforcing a mean-zero $\tilde{\mathbf{b}}_N$, so that the corrected data $\tilde{\mathbf{b}}_{N0}$ are in the column space of \mathcal{L}_N .*

There are many possible approaches to enforce the compatibility condition, which will be explored in detail in future studies, but the simplest choice is perhaps to enforce a mean-zero $\tilde{\mathbf{b}}$ by centering the data:

$$\tilde{\mathbf{b}}_{N0} = \tilde{\mathbf{b}}_N - \bar{\tilde{\mathbf{b}}}_N, \quad (21)$$

and solve $\mathcal{L}_N \mathbf{p} = \tilde{\mathbf{b}}_{N0}$ using CG. $\bar{\tilde{\mathbf{b}}}_N$ is the mean of the contaminated data $\tilde{\mathbf{b}}_N$, and the corrected data $\tilde{\mathbf{b}}_{N0}$ is mean-zero. This simple regularization is effective as $\tilde{\mathbf{b}}_{N0} \in \text{Col}(\mathcal{L}_N)$ and (21) facilitate a consistent system without any regularization to \mathcal{L}_N (see (15) and the short analysis after). In fact, this ‘trick’ is not new but exists in the folklore of the numerical community, which sometimes is used when dealing with high round-off errors. We pen it here not only for housekeeping purposes, but as a reminder that this trick can fix the incompatibility that is critically pronounced in the experimental applications, where the error from experiments is typically much higher than that of round-off errors.

Although simple and effective in enforcing compatibility, this regularization method may be somewhat ‘blunt’, and it does not guarantee the best results. It performs indiscriminate correction to \tilde{f} and \tilde{g}_n that is embedded in $\tilde{\mathbf{b}}_N$ and as a result, this adjustment may ‘correct’ something that should not be corrected. We will demonstrate this in the following section.

Note 7.2 (solve normal equation). *Solve the normal equation instead of the original system (see Remark 4.4) using, for example, CG.*

This is an alternative regularization method to derive a consistent system other than the trick leveraging the divergence theorem (see Note 6.1) or the mean-zero regularization (see Note 7.1) suggested above.

Note 7.3 (use SVD for pseudoinverse). *If computing power allows, use the Singular Value Decomposition to compute the Moore-Penrose pseudoinverse.*

The most robust way to compute MNLS is perhaps to use SVD, which is also a foundational tool to study generalized inverse (Campbell and Meyer, 2009). For example, MATLAB’s `pinv()` function returns Moore-Penrose pseudoinverse using SVD: let the SVD for \mathcal{L}_N is $\mathcal{L}_N = USV^\top$, $\mathcal{L}_N^\dagger = VS^{-1}U^\top$. In addition to being exact, SVD allows a low-rank approximation to \mathcal{L}_N^\dagger , and resulting pressure reconstruction based on which can be smoother and more robust upon a proper choice of rank.

Note 7.4 (early-stopping for CG). *If one somehow has to use the CG to solve an inconsistent and indefinite problem (e.g., (16)), terminating the iterations early is essential.*

This is presumably the practice of Zigunov and Charonko (2024b), which is effective in their tests; however, an optimal stopping criterion is not obvious: one should drive the residual as low as possible before the iteration diverges (see Lim et al. (2024) for an in-depth discussion on the performance of CG and other common iterative solvers on an indefinite inconsistent system). This recent work indicates that CG is numerically unstable for inconsistent systems and it is not guaranteed to give a pseudo-inverse solution.

Note 7.5 (use a CR or MINRES solvers). *Use a proper iterative solver, such as the Conjugate Residual (CR) or a minimum residual (MINRES) solver to solve the inconsistent (16) to ensure a converged solution.*

The key advantage of CR is that the norm of the residuals is monotonically decreasing, and it converges to the normal solution for an inconsistent system. Simple projection at the termination allows CR to recover the pseudo-inverse solution without diverging (see Algorithm 4 in Lim et al. (2024)). A MINRES solver enjoys the same monotonic convergence.

Note 7.6 (use good initial guess and preconditioning). *If an iterative solver is used, there are two common strategies to accelerate the computation: starting the iteration from a good initial guess and/or applying preconditioning.*

The former is particularly relevant to the reconstruction based on time-resolved data. Using the pressure field of the previous instant as the initial guess for the computation of the current time instant can significantly speed up the reconstruction, as the pressure fields at adjacent moments are temporarily correlated and can share a high degree of similarity. An example practice can be found in Chen and Ye (2024). The latter, preconditioning, is generically effective and sometimes can achieve improved numerical stability in addition to the benefits of acceleration. For example, in the following section, we show the performance of CG with incomplete LU (ILU) preconditioning as an example.

8 Validation and Demonstration

While some of the arguments (remarks and notes) can be validated by cross-referencing the tests in the existing literature (Liu and Katz, 2006; Zigunov and Charonko, 2024a,b; Liu and Moreto, 2020; Zhang et al., 2022), we will also provide an independent but unified numerical experiments to demonstrate key points of our arguments.

8.1 ODI \equiv PPE

In this section, we provide direct numerical evidence on the equivalency between RPR-ODI and the PPE for pressure reconstruction. To do this, we use the analytical solution of the Taylor vortex (?) as the ground truth data. The pressure of the vortical flow, p , is calculated as

$$p = -\frac{\rho H^2}{64\pi^2 \nu t^3} \exp\left(-\frac{r^2}{2\nu t}\right), \quad (22)$$

where H represents the angular moment of the vortex, ν the kinematic viscosity of the fluid, ρ the density of the fluid, t the time, and r the distance from the center of the vortex in polar coordinates. We choose the parameters so that the characteristic length scale of the vortex is $L_0 = \sqrt{2\nu t} = 1$ and the leading coefficient (i.e., the amplitude of the characteristic pressure for this flow) is $P_0 = \frac{\rho H^2}{64\pi^2 \nu t^3} = 1$.

The vortex is centered at $(x/L_0, y/L_0) = (-0.5, 0)$ in a $2L_0 \times 2L_0$ domain. The domain is discretized on a uniform 41×41 grid with a grid spacing $h/L_0 = 0.05$. To generate the synthetic data for this experiment, the ground truth pressure (p) and the pressure gradients (\mathbf{g}) are computed based on (22). The synthetic data of the contaminated pressure gradients ($\tilde{\mathbf{g}}$) are generated by adding mean-zero Gaussian noise with a standard deviation of $\sigma_{\mathbf{g}} = 0.5P_0/L_0$ to the components of $\tilde{\mathbf{g}}$ independently. Note that the characteristic pressure gradient for this flow is $P_0/L_0 = 1$ meaning

this artificial noise is rather high. The noisy data for the PPE is calculated using the noisy pressure gradient and the pressure is then reconstructed using both the RPR-ODI and PPE.

For the RPR-ODI, the ray rotation increment is set to be $\Delta\alpha = 0.15$ or 0.5 , and the ray spacing is $\delta r/L_0 = 0.025$, resulting in normalized ray spacing $\Delta d^* = \delta r/h = 0.5$. This choice of the hyperparameters presumably facilitates a high-resolution setting ($\Delta\alpha \approx 0.1 - 0.2^\circ$ and $0.35 < \Delta d^* < 0.71$) recommended by Liu and Moreto (2020) for accurate reconstruction based on RPR-ODI. The tolerance of the RPR-ODI iteration is set to be 10^{-10} and the maximum iteration is $n_{\text{itr}} = 20$. Starting from an initial guess of $p = 0$, RPR-ODI typically converges in about 10 steps. The computed pressure is then shifted to match the ground truth at a corner of the domain (i.e., $(x/L_0, y/L_0) = (-1, -1)$).

For the PPE, a finite difference approximation is used with all Neumann boundary conditions and the particular stencils shown in Sect. 2. The resulting singular but consistent system of equations of (16) was solved using both MATLAB’s pseudo-inverse (i.e., `pinv()`) and a CG solver with tolerance being $\text{tol} = 10^{-8}$ and maximum iteration of $n_{\text{itr}} = 41^2 = 1681$ which is the dimension of \mathcal{L}_N . We dub these two PPE solvers as PPE-PINV and PPE-CG herein. Similar to the use of RPR-ODI, the solutions from PPE were shifted to match the pressure ground truth at $(x/L_0, y/L_0) = (-1, -1)$. The aforementioned procedure was then repeated a total of 500 times each with independently generated random noise and compared for a statistical test.

Figure 2 demonstrates the typical and statistical performance of the solvers. In Fig. 2(e), we show the correlations of the results (i.e., pressure reconstruction \hat{p} and the error in the pressure reconstruction ϵ_p) by RPR-ODI and PPE solved by Moore-Penrose pseudo-inverse. The correlations are computed as

$$R = \frac{\text{Cov}[X_{\text{ODI}}, X_{\text{PPE}}]}{\sqrt{\text{Var}[X_{\text{ODI}}]\text{Var}[X_{\text{PPE}}]}},$$

where X represents the reconstructed pressure or the error in the reconstructed pressure. In our tests, the mean of the 500 correlations for the pressure reconstructions is $R(\hat{p}) = 0.9998$ for $\Delta\alpha = 0.5$ and 0.15 . This suggests that the pressure reconstructed by RPR-ODI and PPE solved by pseudo-inverse is practically identical, which validates the equivalency of ODI and PPE argued in Sect. 2. The mean of the reconstruction error correlation is $R(\epsilon_p) = 0.9653$ and 0.9654 , which are also high. This further supports the ODI \equiv PPE argument. A set of typical pressure reconstructions using RPR-ODI, PPE solved by pseudo-inverse and CG based on the same data out of 500 tests are illustrated in Fig. 2(b–d), respectively. The corresponding error maps in the reconstructed pressure field are shown in Fig. 2(g–i), respectively. Both the pressure fields and the error maps are virtually identical as expected.

We also notice that $R(\hat{p})$ and $R(\epsilon_p)$ are not precisely unity (indicating perfect similarity). This may be due to the numerical implementation details of the methods. For example, to conduct an RPR-ODI, one must choose extra hyperparameters such as the ray rotation angle increment, ray spacing, tolerance, and maximum number of iterations, while PPE solved by pseudo-inverse could be implemented using different stencils and different algorithms for pseudo-inverse (e.g., the results from SVD or COD-based algorithms, or some iterative solvers such as CG or GR are not exactly the same). In addition, the low spatial resolution of data in these tests, adopted to accommodate the high computational cost of mass trials for RPR-ODI, may also contribute to the slight spread in the correlations.

The three boxes in Fig. 2(f) show the statistics of the reconstruction error based on 500 independent tests using RPR-ODI (A), PPE solved by SVD-based pseudo-inverse (B), and PPE solved by CG (C). The statistics of the errors are very similar; however, the reconstruction based on the PPE is slightly better than that from the RPR-ODI. This can be seen by observing the sample

mean and standard deviation of the errors in the reconstructed pressure as shown in Table 1. The slightly lower mean and variance of the reconstruction error in PPE-based solvers suggest that, with the same underlying numerical differentiation scheme, the PPE-based solvers could achieve greater accuracy and precision compared to those based on ODI.

In addition, we want to point out that some minor modifications could effectively improve the performance of PPE-based solvers. For example, using a larger stencil to discretize the Laplacian (Zigunov and Charonko, 2024a; Zigunov and Pan, 2024) or using weighted least squares (Zhang et al., 2020) can achieve around 5% – 20% improvement in terms of reconstruction accuracy in their tests, compared to the ODI or PPE solvers. We will leave a systematic discussion on this topic to future studies.

Table 1: The statistics (sample mean and standard deviation) of the reconstruction error for RPR-ODI, PPE-PINV, and PPE-CG. The hyperparameters for RPR-ODI are $\Delta d^* = 0.5$ and $\Delta\alpha = 0.5$ or 0.15 . The error distribution for the case of $\Delta\alpha = 0.5$ is shown in Fig. 2(f).

Statistics	$\Delta\alpha$	RPR-ODI (A)	PPE-PINV (B)	PPE-CG (C)
$\mathbb{E}[\ \epsilon_p\ _{L^2(\Omega)}]/P_0$	0.5°	3.84×10^{-2}	3.73×10^{-2}	3.73×10^{-2}
	0.15°	3.78×10^{-2}		
σ_{ϵ_p}/P_0	0.5°	1.76×10^{-2}	1.67×10^{-2}	1.67×10^{-2}
	0.15°	1.72×10^{-2}		

8.2 Compatibility and Stable Computing of PPE

We use a snapshot of a two-dimensional Taylor-Green vortex as another ‘minimal example’ to demonstrate the importance of having compatible data and to showcase some of the associated critical nuances for stable computation.

The two components of the velocity field of the Taylor-Green vortex are $u = U_0 \sin(\pi x/L_0) \cos(\pi y/L_0)$ and $v = -U_0 \cos(\pi x/L_0) \sin(\pi y/L_0)$, where U_0 and L_0 are the characteristic velocity and length, respectively. The pressure field is $p = \frac{1}{2}P_0 [\cos(2\pi x/L_0) + \cos(2\pi y/L_0)]$, where $P_0 = \frac{1}{2}\rho U_0^2$ is the characteristic pressure and ρ is the density of the fluid. In our tests, we set L_0 , U_0 , and ρ to unity. The vortex is centered within a $x/L_0 \times y/L_0 \in [0, 1] \times [0, 1]$ domain and discretized on a uniform 126×126 grid with a grid spacing $h/L_0 = 0.008$.

The uncontaminated pressure gradient \mathbf{g} is calculated from the ground truth p , and then the uncontaminated data f is calculated from \mathbf{g} . To generate synthetic corrupted data, this time, however, independent mean-zero Gaussian noise with a constant standard deviation (i.e., $\sigma_{u,v}/U_0 = 0.03$) are added to the ground truth velocity components. The contaminated pressure gradient $\tilde{\mathbf{g}}$ is calculated from the contaminated velocity \tilde{u} and \tilde{v} . Lastly, the contaminated data \tilde{f} is computed from the noisy pressure gradient $\tilde{\mathbf{g}}$.

With the synthetic data prepared, we reconstructed the pressure field by solving the PPE using one point Dirichlet boundary condition at the corner $(x/L_0, y/L_0) = (0, 0)$. This ‘canonical’ simple practice results in a mathematically well-posed problem, but it carries the risk of unstable reconstruction if not handled carefully, especially when the data are contaminated. We organized four different tests by slightly varying the use of data and regularization to reveal the subtle importance of the compatibility and demonstrate some arguments in Sect. 6 and 7.

For the first test (test I), we solve the PPE using both the contaminated data (\tilde{f}) and the pressure gradients ($\tilde{\mathbf{g}}_n$) on the boundaries as Neumann conditions, this will act as a baseline. \tilde{f} is

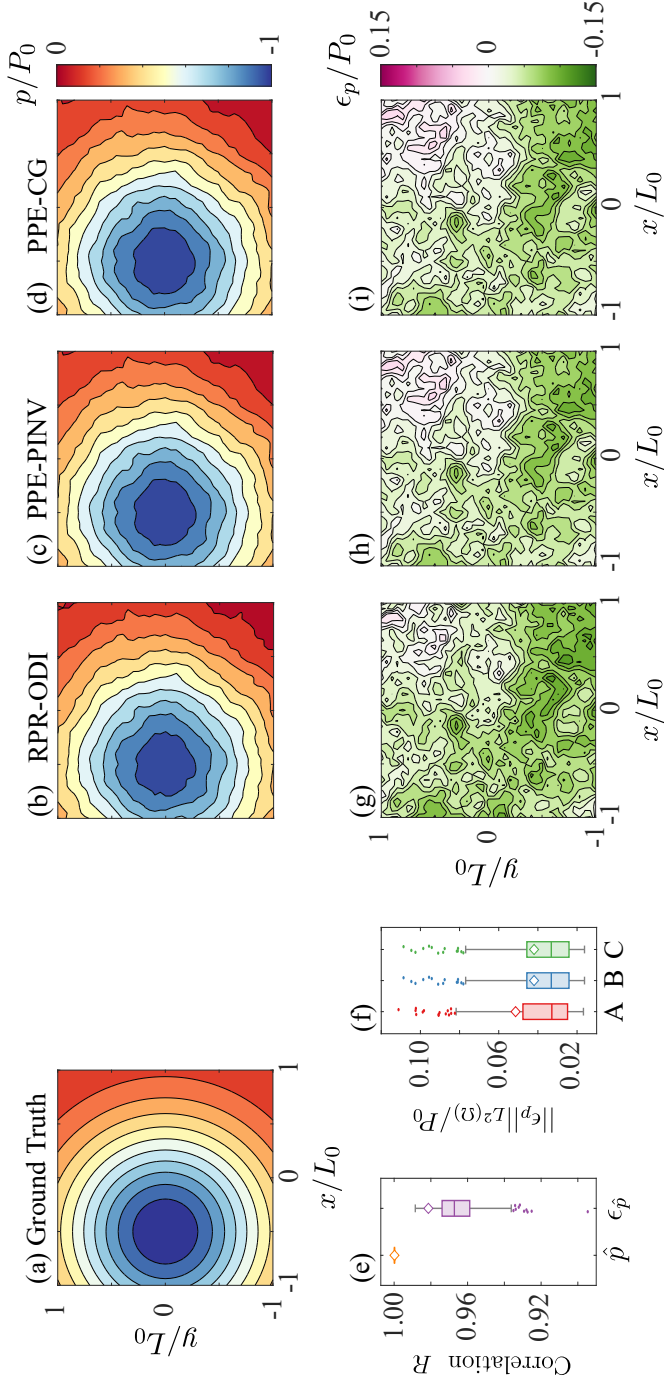


Figure 2: Comparison of ODI and PPE: (a) pressure field ground truth, pressure reconstructed using RPR-ODI (b), incompatible PPE by pseudo-inverse (c) and CG (d), respectively; (g-i) error in the pressure reconstruction by comparing (b-d) with (a) respectively. (e) Box plots of pressure reconstruction (\hat{p}) and error in the pressure (ϵ_p) correlation between RPR-ODI and PPE solved using pseudo-inverse respectively; (f) Box plots for the space-averaged L^2 -norm of the error in the pressure reconstruction by RPR-ODI (A), PPE-PINV (B) and PPE-CG (C), respectively. Box plots (e & f) are based on 500 independent tests. Horizontal bars in the middle of the boxes show the median while the upper and lower edges of the box indicate the 25 and 75 percentiles. The upper and lower whiskers bound the 95% confidence intervals of the error while the diamond symbols within the boxes mark where the corresponding tests shown in (b-d and g-i) lie within the data.

directly computed based on $\tilde{f} = \nabla \cdot \tilde{g}$ (see Note 6.1), and thus, the resulting system is compatible. The linear system for this test and the rest three, take the form of (20) and are solved using MATLAB’s `mldivide()`. Note, (20) is definite and invertible, and we don’t need to solve it by pseudo-inverse.

For the second test (test II), we solve the PPE using the contaminated data \tilde{f} , but this time using g_n , the uncontaminated pressure gradients on the boundary for Neumann conditions. Conventional wisdom may suggest that error-free boundary conditions should yield better results. However, as we will soon see, compatibility issues between g_n and \tilde{f} prevent this from being the case.

For the third test (test III), we use the same contaminated data (\tilde{f}) and error-free Neumann boundaries (g_n), but this time we correct the data (\tilde{b}) such that it is mean zero before adding in the Dirichlet condition at the corner. This is the regularization suggested by (21) in Note 7.1.

For the last test (test IV), we again use the contaminated data (\tilde{f}) and error-free Neumann boundaries (g_n), however, this time we take full advantage of the high-quality gradient data on the boundary while making sure to preserve compatibility. To do this, we construct a corrected pressure gradient field \tilde{g}_c , such that \tilde{g}_c is equal to the error-free pressure gradient g_n on the boundaries, and equal to the noisy gradient \tilde{g} that yields compatible \tilde{f} in the domain. A such \tilde{g}_c can be achieved by simply replacing \tilde{g} on the boundary with g_n . From this corrected pressure gradient \tilde{g}_c , we compute the corrected data $\tilde{f}_c = \nabla \cdot \tilde{g}_c$ per the suggestion in Note 6.1. We then solve the PPE using the corrected data \tilde{f}_c and the error-free Neumann condition g_n with the one-point Dirichlet condition. In most cases, accurate Neumann conditions are not easy to obtain except for some special applications (e.g., internal flows enclosed by walls, where $g_n = 0$ at walls can be considered accurate Neumann boundaries). However, this test serves as a hypothetical demonstration that careful setup of the computation is needed and specific best practices are often problem-dependent.

Figure 3 shows the results from the aforementioned four tests. Each test was repeated 500 times with independently generated random noises with the same statistics introduced to the velocity field. The error in the reconstructed pressure field from the four tests are shown by the four boxes in Fig. 3(f). In the red box (I), the reconstructed error is rather low, despite that both the data and the boundary conditions are contaminated (see Fig. 3(b&g) for a typical reconstructed pressure field and the corresponding error map). This preferred performance is attributed to leveraging the divergence theorem as suggested in Note 6.1 to ensure the compatibility condition of the underlying Neumann problem: any consistent numerical scheme for $\tilde{f} = \nabla \cdot \tilde{g}$ guarantees that $\int_{\Omega} \tilde{f}$ (total generation in the domain) is compatible with $\int_{\partial\Omega} \tilde{g}_n$ (flux on the boundary).

As shown in the blue box (II) in Fig. 3(f), the errors from test II are particularly high despite error-free boundary conditions being used. This may be counter-intuitive as using more accurate data is seemingly counterproductive; however, the real reason for this ‘failure’ is that \tilde{f} and g_n are not compatible: $\int_{\Omega} \tilde{f} dV - \int_{\partial\Omega} g_n dS = \epsilon_c \neq 0$. The unbalanced generation (the none-zero ϵ_c) must go through the Dirichlet boundary (one point in our case). Depending on the value of ϵ_c and the length of the Dirichlet boundaries, the ‘flux’ or the pressure gradient near the Dirichlet boundaries can be excessively high. In the case of our test, the pressure value at the $(x/L_0, y/L_0) = (0, 0)$ corner is anchored and the steep gradient near this corner shifts the entire pressure field, leading to significant errors in the reconstruction. This effect is exemplified in Fig. 3(c&h), where the reconstructed pressure appears to have a high ‘constant’ offset, except at the Dirichlet point where the pressure value remains exact.

The regularization used in test III resolves this compatibility issue and the corresponding high reconstruction error. As shown in Fig. 3(f), the green box (III) is significantly lower than the blue box (II) with reconstruction error being around $\epsilon_p/P_0 \approx 10\%$. However, the solution from this ‘blunt’ regularization is slightly distorted as shown in a typical pressure field and the corresponding error (Fig. 3(d) and (i), respectively). This is due to the fact that we have inadvertently adjusted

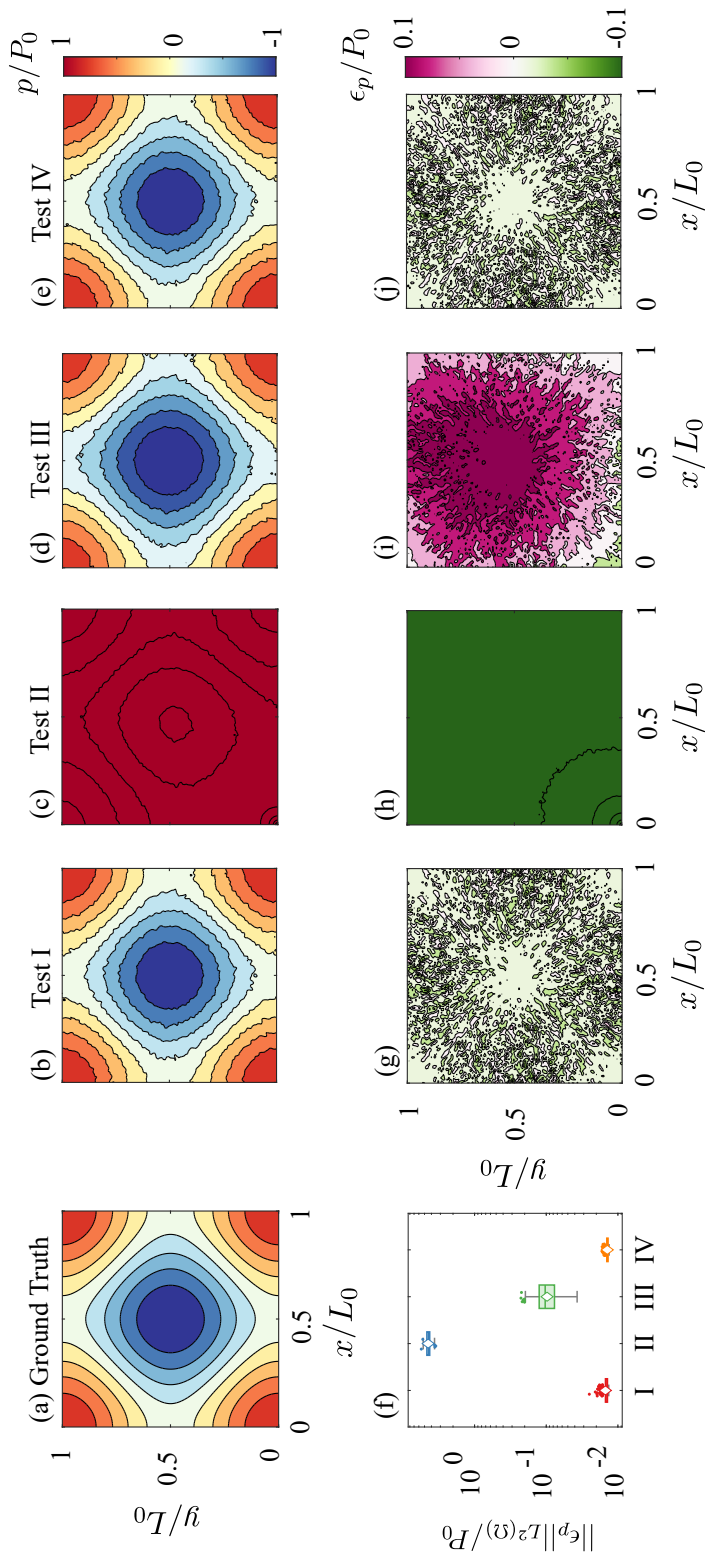


Figure 3: Comparison of incompatible vs compatible data: (a) pressure field ground truth (b–e) reconstructed pressure using \tilde{g}_n and \tilde{f} following Note 6.1, g_n and \tilde{f} , and \tilde{g}_n and \tilde{f} with mean-zero data correction (see Note 7.1), g_n and \tilde{f}_c following Note 6.1 respectively; (g–j) error in the reconstructed pressure field by comparing (b–e) with (a), respectively; (f) Box plot of error in the pressure reconstruction from 500 independent tests with the red (I), blue (II) green (III), and orange (IV) boxes for the statistics of the error due to the use of different methods and data (corresponding to the description for (b–e), respectively). Horizontal bars in the middle of the boxes show the median while the upper and lower edges of the box indicate the 25 and 75 percentiles. The upper and lower whiskers bound the 95% confidence intervals of the error while the diamond symbols within the boxes mark where the corresponding error shown in (g–j) lie within the data.

both the contaminated data (\tilde{f}) and the error-free boundaries (g_n). The cost of the simplicity of this blunt regularization, although it ensures global compatibility, consists of two parts: i) the exact error-free boundary conditions are slightly adjusted by the regularization, which is no longer accurate; and error on the Neumann boundaries can significantly affect pressure reconstruction (Faiella et al., 2021; Sperotto et al., 2022) and ii) the local compatibility may not be satisfied for subdomains that share the boundary with the domain.

In addition, one may notice that the error represented by the green box (III) is higher than that of the red box (I), despite that regularization with error-free Neumann boundary is utilized. This suggests that a more careful approach is necessary, as when the contribution from the error on the boundary is absent, the total error in reconstructed pressure should be lower, especially for a small domain (Pan et al., 2016; Pryce et al., 2024).

The approach proposed in test IV is effective as shown in the orange box (IV) in Fig. 3(f). The practice suggested by Note 6.1 grants the global and local compatibility between \tilde{f}_c and error-free g_n , while the reconstructed pressure field exactly satisfies the accurate Neumann conditions g_n . The superior performance can also be seen in Fig. 3(e&j), while the pattern of the error is similar to that in the test I (see Fig. 3(b&g)). The statistics of the reconstruction error show the expected error for test IV is lower than that for test I and test IV enjoys significantly lower variance (see Table 2). This recovered our intuition that proper use of accurate data can improve the accuracy and precision of the estimation.

With the sample mean ($\mathbb{E}[\|\epsilon_p\|_{L^2(\Omega)}]$) and standard deviation (σ_{ϵ_p}) of the error in the reconstruction, we may estimate the upper bound of the error $\|\epsilon_p\|_{L^2(\Omega)}$ using the 3-sigma rule. That is $\|\epsilon_p\|_{L^2(\Omega)} \lesssim \mathbb{U}[\|\epsilon_p\|_{L^2(\Omega)}]$, where $\mathbb{U}[\|\epsilon_p\|_{L^2(\Omega)}] = \mathbb{E}[\|\epsilon_p\|_{L^2(\Omega)}] + 3\sigma_{\epsilon_p}$ is an estimated upper bound, which is presumably an uncertainty estimate. In Table 2, we also list the upper bound estimates for the four tests. It is evident that test IV enjoys the lowest error due to compatible data and accurate boundary conditions, and test test II suffers from high error caused by the singularity at the Dirichlet corner.

Table 2: The sample mean, standard deviation, and the estimate of the upper bound of the reconstruction error in Fig. 3(f).

	Test I	Test II	Test III	Test IV
$\mathbb{E}[\ \epsilon_p\ _{L^2(\Omega)}]/P_0$	1.47×10^{-2}	4.42	1.04×10^{-1}	1.41×10^{-2}
σ_{ϵ_p}/P_0	1.21×10^{-3}	3.14×10^{-1}	3.49×10^{-2}	5.51×10^{-4}
$\mathbb{U}[\ \epsilon_p\ _{L^2(\Omega)}]/P_0$	1.83×10^{-2}	5.36	2.09×10^{-1}	1.58×10^{-2}

8.3 On the Iterative Solvers

To showcase the behaviour of the conjugate gradient solver used by Zigunov and Charonko (2024b) and demonstrate other numerical minutiae related to linear solvers, we perform an additional experimentation where we compare CG and CR subject to compatible and incompatible data. We also show how simple preconditioning can effectively reduce the number of iterations required for convergence. In this numerical experiment, we employ the same Taylor vortex used in the previous numerical test in Sect. 8.1 with the same all Neumann domain and discretization. The contaminated pressure gradient and the data are also generated in a similar manner. To construct a compatible problem we use the data \tilde{f} computed from contaminated gradient \tilde{g} . For the incompatible case we use the error-free Neumann boundary conditions g_n and the noisy data \tilde{f} , which is similar to the practice for test II in Sect. 8.2. The PPE is then solved using CG and CR for both the compatible

and incompatible data from an initial guess of $p = 0$ with the tolerance being $\text{tol} = 5 \times 10^{-14}$ and maximum iteration of $n_{\text{itr}} = 41^2 = 1681$ again matching the dimension of \mathcal{L}_N . Lastly, we also tested the Incomplete LU (ILU) preconditioned CG (PCG) on compatible data. The results of this experiment can be seen in Fig. 4.

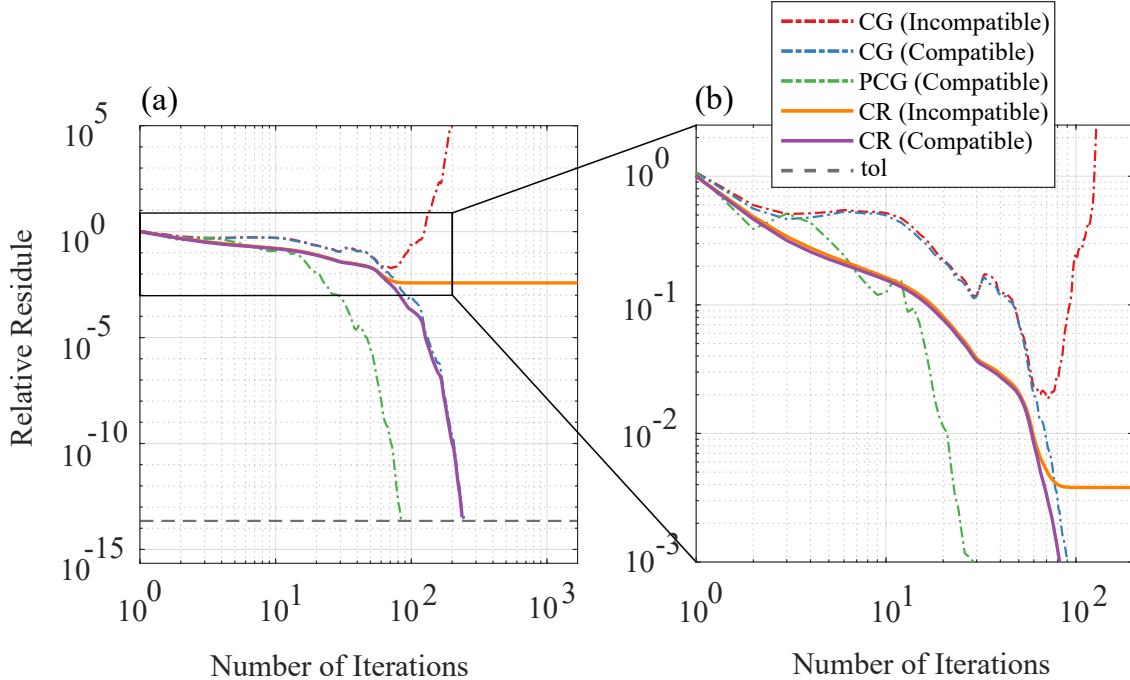


Figure 4: Behavior of iterative solvers (CG, CR, and Preconditioned CG (PCG)) using ILU on compatible and incompatible linear systems derived from the PPE (a). Zoom-in of the designated part of (a).

Figure 4 depicts the relative residual ($\|\mathcal{L}_N \hat{\mathbf{p}}_k - \mathbf{b}\|_2 / \|\mathbf{b}\|_2$) of the solution $\hat{\mathbf{p}}_k$ over the number of iterations k . As shown in Fig. 4, CR is unconditionally stable independent of the compatibility of the system (purple and orange solid lines). This is a critically favourable property as the solution is assured to not blow up. Thus, we recommend to use CR as the iterative solver (see Note 7.5) for robust computation, especially when the consistency of the system is not known. For a compatible system, CR can converge to a small tolerance (almost machine precision). For an incompatible system, the residual of the CR algorithm plateaus above the small target tolerance. This is expected, as the ‘exact’ solution to an incompatible system does not exist; instead, CR converges to the MNLS solution, which is the same as the solution from the Moore-Penrose pseudo-inverse (Lim et al., 2024).

The behaviour of CG depends on the compatibility of the system. On a compatible but indefinite system, CG is guaranteed to converge to the minimal norm solution of the problem (see the blue chain line in Fig. 4), which is a well-established result (Kammerer and Nashed, 1972; Hestenes, 2012; Lim et al., 2024). Preconditioning can accelerate the solution (see the green chain line in Fig. 4 and Note 7.6). For an inconsistent and indefinite system, there is no guarantee that CG will not diverge after many enough iterations (see Lim et al. (2024) for analysis). This is evident by observing the red chain line in Fig. 4. For the particular problem in our test, CG diverges after about 60 iterations. However, before divergence, CG on the inconsistent and indefinite system converges *towards* the minimal norm solution similar to its behaviour on a compatible system. Thus, if one has to use CG on an inconsistent and indefinite system, early-stop is essential (see Note 7.4). Otherwise, some regularization should be applied to make the problem compatible.

Despite the many possible options for regularization, some of the elementary choices suggested in this work are perhaps the easiest to implement and are effective in terms of ensuring compatibility (see e.g., Notes 6.1, 7.1, and 7.2).

9 Concluding Remarks and Perspectives

With straightforward numerical treatment based on the work by [Zigunov and Charonko \(2024b\)](#), we show that the Rotating Parallel Ray Omnidirectional Integration (RPR-ODI) is equivalent to pursuing the Minimum Norm Least Squares (MNLS) solution to the Pressure Poisson Equation (PPE) with all Neumann boundary conditions. In doing so, we hope to put an end to the PPE versus ODI debate and clear up the confusion surrounding why and when these methods perform well. By examining image velocimetry based pressure field reconstruction—a classic challenge in experimental fluid mechanics—through the perspectives of the Poisson equation’s well-posedness, linear algebra, estimation, and optimization, we provide insights into the strengths and limitations of conventional ODI methods ([Liu and Moreto, 2020](#)), matrix ODI methods ([Zigunov and Charonko, 2024a,b](#)), and select PPE-based solvers ([McClure and Yarusevych, 2017b](#); [Zhang et al., 2020](#)).

We demonstrate that the key to successfully reconstructing the pressure field using ODI/PPE based on image velocimetry data lies in either i) formulating a problem with an underlying compatible Neumann problem, or ii) solving the corresponding inconsistent and indefinite system by pursuing the MNLS solution. Both approaches ensure a well-posed and robust reconstruction. This understanding may inspire new regularization and data assimilation techniques or improve existing ones to further enhance the quality of pressure field reconstruction.

Before closing, we want to emphasize on two fundamental limitations and potential improvements of the conventional or matrix ODI algorithms as well as their equivalent PPE-based pressure solvers. First, given the fact that the error in the particle image velocimetry is usually correlated, the uncertainty in the domain is spatially inhomogeneous, and the error in the pressure gradient is not necessarily mean-zero, the reconstruction from this family of solvers does not grant the best linear unbiased estimator (minimizing the bias), or any estimator that minimizing the variance (i.e., uncertainty). Instead, the MNLS solution is sub-optimal from a statistical perspective, and improvements to ODI/PPE can be readily achieved by applying established results in statistics and classical estimation theory. Second, ODI is motivated by the intention of enforcing the curl-free property for a corrupted pressure gradient field; however, the equivalency between the ODI and PPE shows that the curl-free correction goal is not achieved. Thus, a pressure solver that properly incorporates curl-free correction could yield better results than the ODI and equivalent PPE-based solvers. Some existing works (e.g., [Wang et al. \(2016\)](#); [McClure and Yarusevych \(2017a\)](#); [Wang et al. \(2017\)](#); [McClure and Yarusevych \(2019\)](#); [Lin and Xu \(2023\)](#); [Li et al. \(2024b\)](#)) can be seen as an improvement from this regard.

Last, in terms of computational efficiency, [Zigunov and Charonko \(2024a,b\)](#) already dramatically reduced the prohibitive computational cost of the conventional ODI to the level of PPE. However, we recognize that the computational performance demonstrated in [Zigunov and Charonko \(2024a,b\)](#) and in the current work has room for improvement, as fast Poisson solvers remain an active area of research despite extensive existing results. By establishing the equivalence between ODI and PPE in the current work, we can enhance the computational efficiency of ODI or its equivalent PPE by leveraging the extensive literature on fast solvers for elliptic equations and robust numerical linear solvers.

For now, we conclude the first part of our work on this topic, which primarily establishes the equivalence between ODI and PPE. Further studies on potential improvements will follow.

References

- Campbell, S. L. and Meyer, C. D. (2009). *Generalized inverses of linear transformations*. SIAM.
- Charonko, J. J., King, C. V., Smith, B. L., and Vlachos, P. P. (2010). Assessment of pressure field calculations from particle image velocimetry measurements. *Measurement Science and Technology*, 21(10):105401.
- Chen, L. (2020). Lecture notes. <https://www.math.uci.edu/~chenlong/lectures.html> [Accessed: 2024-02-15].
- Chen, L. and Ye, Q. (2024). Piv-based fast pressure reconstruction and noise prediction of tandem cylinder configuration. *Experiments in Fluids*, 65(6):98.
- Dabiri, J. O., Bose, S., Gemmell, B. J., Colin, S. P., and Costello, J. H. (2014). An algorithm to estimate unsteady and quasi-steady pressure fields from velocity field measurements. *Journal of Experimental Biology*, 217(3):331–336.
- De Kat, R. and Van Oudheusden, B. (2012). Instantaneous planar pressure determination from PIV in turbulent flow. *Experiments in fluids*, 52(5):1089–1106.
- Faiella, M., Macmillan, C. G. J., Whitehead, J. P., and Pan, Z. (2021). Error propagation dynamics of velocimetry-based pressure field calculations (2): on the error profile. *Measurement Science and Technology*, 32(8):084005.
- Gallier, J. and Quaintance, J. (2020). *Linear Algebra and Optimization with Applications to Machine Learning: Volume I: Linear Algebra for Computer Vision, Robotics, and Machine Learning*. World Scientific.
- Hastie, T., Tibshirani, R., Friedman, J. H., and Friedman, J. H. (2009). *The elements of statistical learning: data mining, inference, and prediction*, volume 2. Springer.
- Henderson, C. R. (1975). Best linear unbiased estimation and prediction under a selection model. *Biometrics*, pages 423–447.
- Hestenes, M. R. (2012). *Conjugate direction methods in optimization*, volume 12. Springer Science & Business Media.
- Hoerl, A. E. and Kennard, R. W. (1970). Ridge regression: Biased estimation for nonorthogonal problems. *Technometrics*, 12(1):55–67.
- Kammerer, W. J. and Nashed, M. Z. (1972). On the convergence of the conjugate gradient method for singular linear operator equations. *SIAM Journal on Numerical Analysis*, 9(1):165–181.
- Li, L., McClure, J., Wright, G. B., Whitehead, J. P., Wang, J., and Pan, Z. (2024a). Error propagation of direct pressure gradient integration and a helmholtz-hodge decomposition based pressure field reconstruction method for image velocimetry. *arXiv preprint arXiv:2407.15344*.
- Li, L., McClure, J., Wright, G. B., Whitehead, J. P., Wang, J., and Pan, Z. (2024b). Error propagation of direct pressure gradient integration and a helmholtz-hodge decomposition based pressure field reconstruction method for image velocimetry. *arXiv preprint arXiv:2407.15344*.
- Lim, A., Liu, Y., and Roosta, F. (2024). Conjugate direction methods under inconsistent systems. *arXiv preprint arXiv:2401.11714*.

- Lin, Y. and Xu, H. (2023). Divergence–curl correction for pressure field reconstruction from acceleration in turbulent flows. *Experiments in Fluids*, 64(137).
- Liu, X. and Katz, J. (2003). Measurements of pressure distribution by integrating the material acceleration. In *Cav03-GS-14-001, Fifth international symposium on cavitation (CAV2003), Osaka, Japan*, pages 1–4.
- Liu, X. and Katz, J. (2006). Instantaneous pressure and material acceleration measurements using a four-exposure PIV system. *Experiments in Fluids*, 41(2):227–240.
- Liu, X. and Moreto, J. R. (2020). Error propagation from the piv-based pressure gradient to the integrated pressure by the omnidirectional integration method. *Measurement Science and Technology*, 31(5):055301.
- Liu, X., Moreto, J. R., and Siddle-Mitchell, S. (2016). Instantaneous pressure reconstruction from measured pressure gradient using rotating parallel ray method. In *54th AIAA Aerospace Sciences Meeting*, page 1049.
- McClure, J. and Yarusevych, S. (2017a). Instantaneous PIV/PTV-based pressure gradient estimation: a framework for error analysis and correction. *Experiments in Fluids*, 58:1–18.
- McClure, J. and Yarusevych, S. (2017b). Optimization of planar PIV-based pressure estimates in laminar and turbulent wakes. *Exp Fluids*, 58(5):62.
- McClure, J. and Yarusevych, S. (2019). Generalized framework for PIV-based pressure gradient error field determination and correction. *Measurement Science and Technology*, 30(8):084005.
- Pan, Z., Whitehead, J., Thomson, S., and Truscott, T. (2016). Error propagation dynamics of piv-based pressure field calculations: how well does the pressure poisson solver perform inherently? *Measurement Science and Technology*, 27(8):084012.
- Pryce, C., Li, L., Whitehead, J. P., and Pan, Z. (2024). A simple boundary condition regularization strategy for image velocimetry-based pressure field reconstruction. *Experiments in Fluids*, 65(6):1–6.
- Schwabe, M. (1935). Über druckermittlung in der nichtstationären ebenen strömung. *Ingenieur-Archiv*, 6(1):34–50.
- Sperotto, P., Pieraccini, S., and Mendez, M. A. (2022). A meshless method to compute pressure fields from image velocimetry. *Measurement Science and Technology*, 33(9):094005.
- Thomas, J. W. (2013a). *Numerical partial differential equations: conservation laws and elliptic equations*, volume 33. Springer Science & Business Media.
- Thomas, J. W. (2013b). *Numerical partial differential equations: finite difference methods*, volume 22. Springer Science & Business Media.
- Van Oudheusden, B. (2013). PIV-based pressure measurement. *Measurement Science and Technology*, 24(3):032001.
- Wang, C., Gao, Q., Wei, R., Li, T., and Wang, J. (2017). Weighted divergence correction scheme and its fast implementation. *Experiments in Fluids*, 58:1–14.

- Wang, J., Zhang, C., and Katz, J. (2019). Gpu-based, parallel-line, omni-directional integration of measured pressure gradient field to obtain the 3d pressure distribution. *Experiments in Fluids*, 60:1–24.
- Wang, Q. and Liu, X. (2023). Green’s function integral method for pressure reconstruction from measured pressure gradient and the interpretation of omnidirectional integration.
- Wang, Z., Gao, Q., Wang, C., Wei, R., and Wang, J. (2016). An irrotation correction on pressure gradient and orthogonal-path integration for piv-based pressure reconstruction. *Experiments in Fluids*, 57:1–16.
- Zhang, J., Bhattacharya, S., and Vlachos, P. P. (2020). Using uncertainty to improve pressure field reconstruction from piv/ptv flow measurements. *Experiments in Fluids*, 61:1–20.
- Zhang, J., Bhattacharya, S., and Vlachos, P. P. (2022). Uncertainty of piv/ptv based eulerian pressure estimation using velocity uncertainty. *Measurement Science and Technology*, 33(6):065303.
- Zigunov, F. and Charonko, J. J. (2024a). A fast, matrix-based method to perform omnidirectional pressure integration. *Measurement Science and Technology*, 35(6):065302.
- Zigunov, F. and Charonko, J. J. (2024b). One-shot omnidirectional pressure integration through matrix inversion. *Measurement Science and Technology*, 35(6):125301.
- Zigunov, F. and Pan, Z. (2024). Private communication, at humberto delgado airport, lisboa, portugal, july 12, 2024.